Bonding of xenon to oxygen in magmas at depth

Clémence Leroy[1], Chrystèle Sanloup[2*], Hélène Bureau[1],
Burkhard C. Schmidt[3], Zuzana Konôpková[4], Caroline Raepsaet[5]

[1] *Sorbonne Universités, UPMC Univ Paris 06, CNRS,*
Institut de Minéralogie, de Physique des matériaux et de Cosmochimie, 75005 Paris, France
[2] *Sorbonne Universités, UPMC Univ Paris 06, CNRS,*
Institut des Sciences de la Terre de Paris, 75005 Paris, France
[3] *Goettingen University, Geowissenschaftliches Zentrum, 37077 Goettingen, Germany*
[4] *DESY Photon Science, Notkestr. 85, 22607 Hamburg, Germany*
[5] *NIMBE, CEA, CNRS, Université Paris-Saclay, CEA Saclay, 91191 Gif-sur-Yvette, France*

[*] *Corresponding author (chrystele.sanloup@upmc.fr)*

Abstract

The field of noble gases chemistry has witnessed amazing advances in the last decade with over 100 compounds reported including Xe oxides and Xe-Fe alloys stable at the pressure-temperature conditions of planetary interiors. The chemistry of Xe with planetary materials is nonetheless still mostly ignored, while Xe isotopes are used to trace a variety of key planetary processes from atmosphere formation to underground nuclear tests. It is indeed difficult to incorporate the possibility of Xe reactivity at depth in isotopic geochemical models without a precise knowledge of its chemical environment. The structure of Xe doped hydrous silica-rich melts melts is investigated by *in situ* high energy synchrotron X-ray diffraction using resistive heating diamond anvil cells. Obtained pair distribution functions reveal the oxidation of Xe between 0.2 GPa and 4 GPa at high T up to 1000 K. In addition to the usual interatomic distances, a contribution at 2.05±0.05 Å is observed. This contribution is not observed in the undoped melt, and is interpreted as the Xe-O bond, with a coordination number of about 12 consistent

with Xe insertion in rings of the melt structure. Xe solubility measurements by electron microprobe and particle induced X-rays emission analysis confirm that Xe and Ar have similar solubility values in wt% in silicate melts. These values are nonetheless an order of magnitude higher than those theoretically calculated for Xe. The formation of Xe-O bonds explains the enhanced solubility of Xe in deep continental crust magmas, revealing a mechanism that could store Xe and fractionate its isotopes. Xenon is indeed atypical among noble gases, the atmosphere being notably depleted in elemental Xe, and very strongly depleted in Xe light isotopes. These observations are known as the 'missing' Xe paradox, and could be solved by the present findings.

1. Introduction

Noble gases are key tracers of Earth dynamics, and as such, Xe isotopes are important markers of planetary and atmosphere formation (Staudacher and Allègre, 1982; Pepin, 2006); they may also be used to track underground nuclear tests (Hourdin and Issartel, 2000). In particular, the I-Pu-Xe system is used to date the formation of the atmosphere (Ozima and Podosek, 1999; Avice and Marty, 2014) due to the very short half-lifes of ^{129}I (17 My) and ^{244}Pu (82 My). Degassing of the early Earth could thus have massively contributed to the formation of the terrestrial atmosphere within the first 100 Myr (Staudacher and Allègre, 1982). However, recent Monte Carlo simulations pointed out that given the uncertainties on Xe isotopic compositions, such a catastrophic early degassing event could not be evidenced unambiguously, and that the potential chemistry of Xe at depth must be solved first (Boehnke et al., 2015).

Xe abundances and isotopic ratios have been measured in a large variety of samples (atmosphere, fluids, rocks) and from different geological contexts, from Archean rocks (Pujol et al., 2011) to Martian meteorites (Gilmour et al., 1998). From these measurements, it was pointed out as early as 1970 that Xe is missing from the atmosphere of the Earth and Mars (Anders and Owen, 1977), a depletion relative to chondritic patterns of up to 90% (Ozima and Podosek, 1999) and known as the 'missing Xe' problem. Atmospheric Xe is besides strongly depleted in light isotopes (Krummenacher et al., 1962), a depletion that could be even larger if the primordial Earth composition – from which the present-day atmosphere is derived by mass-fractionation processes – is the U-Xe component instead of a solar wind or Q-planetary component (Marty et al., 2017). First high precision measurements of non-radiogenic Xe isotopes (Caffee et al., 1999) and their correlation with $^{129}Xe/^{130}Xe$ ratio showed that the atmosphere was degassed very early after minor iodine decay in the mantle, and then underwent mass fractionation. Three types of scenarios have been proposed to solve the missing Xe problem. (1) Xe may have escaped from the atmosphere, possibly after ionization (Avice and Marty, 2014), (2) Xe may be hidden at depth in the core (Lee and Steinle-Neumann, 2006; Zhu et al., 2014), (3) Xe may have simply not been accreted on the planet (Dauphas, 2003). The fact that Earth and Mars atmospheres are similarly depleted in light Xe isotopes (Swindle et al., 1986) nevertheless points out to a phenomenon that does not depend on the mass of the planet such as hydrodynamic escape or trapping in the deep reservoirs unique to the Earth, i.e. lower mantle and core. Besides, core formation (Kleine et al., 2002) was likely completed by the time Xe was lost around 110 My

(Ozima and Podosek, 1999). Discovery of Archean rocks with Xe isotopic composition falling between primitive chondrites and present Earth atmosphere (Pujol et al., 2011) indicates a storage and fractionation of Xe throughout the Archean that could even continue nowadays through subduction process. Geochemical tracing of Xe recycling in the mantle (Trieloff and Kunz, 2005; Holland and Ballentine, 2006) points indeed to an obvious link between Xe and water intake and release in subduction zones, resulting in the storage of volatiles in the subcontinental lithosphere (Broadley et al., 2016). While natural Xe concentrations are $\sim$0.1 ppt in granites (Allègre et al., 1986) and $\sim$0.05 ppt in basalts (Ozima et al., 2002), they reach 0.2 ppb in deep sea siliceous fossils (Matsuda and Matsubara, 1989) that may later enter subduction zones.

To understand Xe atypical behaviour, the mainstream approach has been to study the relative stability of noble gases in melts relative to the major silicate minerals by measuring partition coefficients. The results (Heber et al., 2007) span 4 orders of magnitude for Ar, and 7 for Xe, mostly due to different interpretations of where the noble gas was incorporated, i.e. exclusively in bubble-free crystal zones or including sub-surface and small bubbles as reflecting gas release upon quenching from high P-T conditions. This highlights the extreme difficulty to probe the behaviour of volatile elements by analyzing samples recovered at ambient conditions, either natural or synthetic. Besides, despite its generally inert nature, Xe has been shown to react with crystalline planetary oxides (Sanloup et al., 2005, 2011, 2013; Seoung et al., 2014; Crépisson et al., 2018) under the high pressure (P)-temperature (T) conditions relevant of planetary interiors. Xe oxides have been synthesized at ambient P and cryogenic T: XeO_3, XeO_4, Xe peroxides

(XeO$_6^{4-}$ ion), XeO$_2$ (Brock and Schrobilgen, 2011), and lately Xe perovskites (Britvin et al., 2016). On the high P side, Xe oxides have been predicted to be stable above 75 GPa (Zhu et al., 2013; Hermann and Schwerdtfeger, 2014), and observed above 77 GPa (Dewaele et al., 2016). Magmas being the most efficient transfer agents, the next natural step was to determine Xe reactivity in silicate melts at depth.

The first and major objective here is to solve the retention mechanisms of Xe in deep silicate melts by means of *in situ* high P-T X-ray diffraction experiments. While X-ray absorption spectroscopy (XAS) is a classical method to probe the local environment of elements in crystals, and used to evidence the Xe-O bond in high P Xe oxides (Dewaele et al., 2016), it is difficult to use it for materials without appropriate standards and with unknown structure, especially disordered materials such as magmas. Instead, X-ray diffraction data are not model dependent. They are however not chemically-selective and all ion-ion contributions must be solved. This implies to work with simplified chemical compositions, such as haplogranitic magmas taken here as analogues of continental crust melts, with only 5 elements (Si, Al, Na, K, and O), and Si making 70 at% of the cations. X-ray diffraction is a well established technique to probe the structural environment of major cations in silicate melts *in situ*, and the recent study of Lu environment in compressed melts has demonstrated its potential to probe the local environment of minor elements (de Grouchy et al., 2017). The second objective is to measure the solubility of Xe in silica-rich melts at high P, current data under high P conditions being limited to the tholeitic composition (Schmidt and Keppler, 2002), and discuss the structural data in the light of Xe solubility measurements

and theoretical estimates.

2. Experimental Methods

2.1. Glass Synthesis

The haplogranite (HPG) glass composition was chosen as a continental crust melt analogue. The starting HPG glass was prepared by mixing reagent grade oxides (Al_2O_3, SiO_2) and carbonates (Na_2CO_3, K_2CO_3) powders. Powder was ground and decarbonated by slow ramp heating from room temperature to 1473 K within 8 hours in a platinum crucible, further fused at 1873 K in an atmospheric furnace for one hour, and quenched in water. The obtained glass was crushed into a powder, and remelted twice at 1873 K to ensure homogeneity. Hydration was done by high P-T synthesis at 2 GPa and 1673 K using a piston-cylinder apparatus with a half-inch talc pyrex assembly, a graphite heater, and dried MgO powder packed around the Pt capsule. Two hydration levels were targeted, 5 wt% and 7 wt%. For that purpose, the glass was encapsulated along with the approximate amount of distilled water in a platinum capsule weld shut at both ends. Xenon doping was done subsequently by gas-loading (Boettcher et al., 1989) another platinum capsule partially filled with the recovered hydrous HPG glasses, and brought to 3.5 GPa and 1873 K for one hour, followed by rapid T quenching and decompression at room T. The major part of the capsule material was used for X-ray diffraction experiments, and a few glass pieces were spared for chemical analysis. The HPG-7wt%H_2O composition was slightly contaminated upon retrieving the hydrated glass from the first platinum capsule by the MgO P-medium packed around the capsule

100 (1.5 wt% MgO, cf Table 1).

101

102 *2.2. Recovered Sample Analysis*

103 Starting glasses and one sample (P5) were analyzed for major elements using a
104 CAMECA SX-FIVE electron microprobe analyzer (EMPA) at Camparis (UPMC, Paris),
105 using a defocused beam of 15 µm diameter and the following operating conditions: 1)
106 15 keV accelerating voltage, 6 nA beam current for Na, K, Al, Si, and 2) 15 keV and 100
107 nA for Xe. Calibration for Xe was established by measuring the counts for the neigh-
108 boring elements, I (CuI) and Cs (CsCl) following the procedure developed by Montana
109 et al. (1993). Hydrogen (i.e. water) and Xe contents were analyzed with the nuclear
110 microprobe of LEEL/LIMBE, CEA Saclay, France using ERDA (Elastic Recoil Detec-
111 tion Analysis) and PIXE (Particle Induced X rays Emission) respectively. For ERDA
112 (Bureau et al., 2009) we used a 4×16 µm^2 incident beam of ^{4}He at 3 MeV, mapped on
113 selected areas (up to 200×200 µm^2). For PIXE (Bureau et al., 2000, 2010), we used a
114 3×3 µm^2 incident beam of protons at 2 MeV mapped on selected areas (up to 200×200
115 µm), and the Xe L X-ray line at 4.1 keV. Xe contents obtained by EMPA (Table 1) and
116 PIXE (Fig.1) compare well, except for one sample (P5) that we attribute to the sample
117 geometry as the sample surface could not be mirror polished, being embedded in the
118 epoxy while still in the rhenium gasket chamber. The PIXE measurements indicate
119 that the sample Xe content did not change during the course of the X-ray diffraction
120 experiment.

Table 1: Chemical composition in wt% obtained from EMPA except * from PIXE and ** from ERDA. Analyses are based on average of 10 data points, standard deviations are shown in brackets.

Oxide	plain glass	Xe-dopped glasses		Recovered sample P5
SiO_2	73.8 (0.6)	69.3 (0.7)	71.3 (0.7)	67.9 (0.9)
Al_2O_3	12.2 (0.3)	11.1 (0.3)	11.7 (0.2)	10.8 (0.3)
Na_2O	4.7 (0.1)	3.6 (0.1)	4.6 (0.1)	3.2 (0.5)
K_2O	4.2 (0.2)	3.7 (0.2)	4.1 (0.2)	3.9 (0.1)
MgO	-	1.5 (0.1)	-	1.6 (0.1)
Xe	-	3.1 (0.2)	4.6 (0.1)	1.5 (0.2)
Xe*	-	3.1 (0.4)	4.0 (0.8)	2.9 (0.4)
H_2O**	5.9 (1.7)	7.2 (2.0)	5.1 (1.4)	7.2 (2.0)
Total	100.8	99.5	100.8	97.5

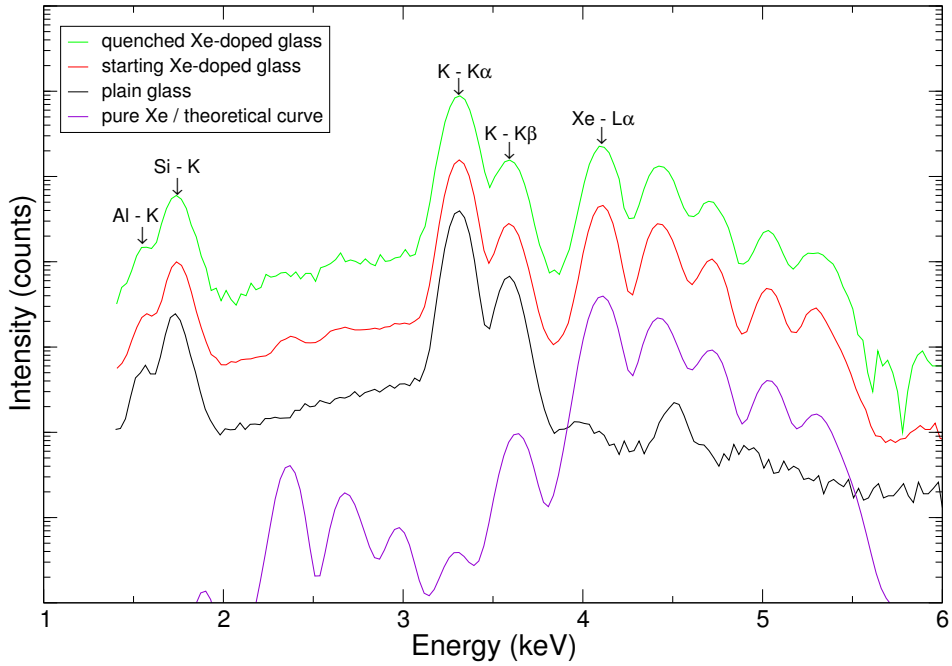

Figure 1: PIXE spectra of glasses and theoretical spectrum. Red line: starting glass (3.1 wt% Xe), green line: glass recovered from XRD run P5 (2.9 wt% Xe).

2.3. X-ray Diffraction

We collected *in situ* high energy synchrotron X-ray diffraction (XRD) data in resistive heating diamond anvil cells at the extreme conditions beamline P02.2, Petra III (DESY, Hamburg). High *P-T* conditions were generated by symmetric resistive-heating diamond-anvil cells (DAC) equipped with either 300 µm culet diamonds and 70°-opening Boehler Almax seats (runs P5, P7, P11) or 800 µm culet diamonds and 80°-opening Boehler Almax seats (runs P3, P6). We used a high energy X-ray monochromatic beam (60 keV) focused down to 4 µm×6 µm to access a wide q-range of 15 $Å^{-1}$ (runs P5, P7, P11) to 16 $Å^{-1}$ (runs P3, P6), allowing high spatial resolution in direct space. While optimising the spatial resolution is always important in structural

studies, it is particularly crucial here to decipher the contribution of Xe, a minor element. Heating was achieved by an internal resistive molybdenum-wire heater, and an external heater set at 200°C around the DAC. The starting glass sample was loaded in a 200 µm diameter hole drilled in a rhenium gasket. Pressure was measured from the fluorescence of a ruby sphere (Mao et al., 1986) at ambient T, and from the unit cell volume of platinum (Fei et al., 2004) at high T. Temperature was read by a type-K thermocouple localized as close as possible to the sample chamber. *In situ* X-ray diffraction data were collected for five different loadings (Table 2 and Fig.2), three on the HPG-3wt%Xe-7wt%H_2O composition, one on the HPG-4wt%Xe-5wt%H_2O composition, and one on the undoped HPG-7wt%H_2O composition. The hydrous HPG composition has a glass transition temperature low enough $\sim$ 850 K (Dingwell, 1998) to be achieved with a resistive heating furnace, and its high silica content (70 at%) implies that the melt is highly polymerized with consequent high noble gases solubility (Carroll and Stolper, 1993). The addition of water to the starting glass consequently lowered the rate of recrystallization upon heating. Recrystallization occurred above the glass transition T in only two runs, while the others remained in the amorphous state, and were quenched as glasses. At each P-T point, 120 times 1 s diffraction patterns were recorded on a Perkin-Elmer 2D detector, and summed. Diffraction patterns were integrated using the Fit2D software (Hammersley et al., 1996). For each run, X-ray diffraction patterns were collected at room conditions with an empty gasket inserted in the DAC. The baseline of the recrystallized patterns (P7 and P11) was used to scale the intensity of the empty background patterns. Obtained patterns were then subtracted

from the sample diffraction patterns to isolate the signal scattered from the melt.

Table 2: Summary of diamond-anvil cell runs.

Run	Starting composition	Quenched products
P3	HPG-7wt%H_2O	glass
P5	HPG-3wt%Xe-7wt%H_2O	glass
P6	HPG-3wt%Xe-7wt%H_2O	glass
P7	HPG-4wt%Xe-5wt%H_2O	crystals
P11	HPG-3wt%Xe-7wt%H_2O	crystals

3. Results

3.1. Overall structural description

To obtain a detailed description of Xe local environment in compressed silicate melt, X-ray diffraction data were collected on both Xe-doped and plain samples as X-ray diffraction is not chemically-selective. All ion-ion contributions must be solved, which could be done in this study due to the chemical simplicity of the chosen magma composition with only 5 elements (Si, Al, Na, K, and O), and Si making 70 at% of the cations. X-ray diffraction intensity data are converted into the structure factor $S(q)$ (Fig.3A), where q is the scattering vector, using the Ashcroft-Langreth formalism. The radial distribution function $g(r)$ (Fig.3B), that describes ion-ion contributions in real

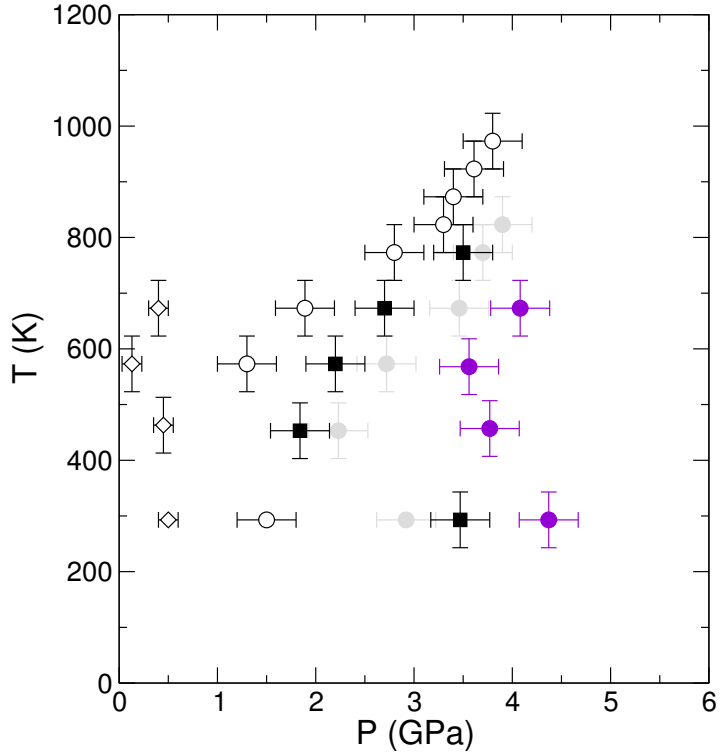

Figure 2: Experimental *P-T* conditions. Circles: HPG-3wt%Xe-7wt%H_2O composition (white: P6, purple: P11, grey: P5); diamonds: HPG-4wt%Xe-5wt%H_2O composition (run P7), dark squares: plain hydrous HPG (P3).

space, is obtained by Fourier transforming of $S(q)$,

$$g(r) = \frac{1}{2\pi^2 rn} \int_0^\infty qS(q) \sin(qr)\, dq \tag{1}$$

where $n = \frac{\rho \mathcal{N}_A}{M}$, M the mean atomic molar mass, and ρ the density calculated using the volumetric properties determined for hydrous rhyolitic liquids (Malfait et al., 2014). Whereas no changes were observed for the plain composition upon heating, an additional contribution is visible at 2.05±0.05 Å above 573 K for the Xe-doped samples, and vanishes upon quenching (Fig.3B). This additional contribution is observed for all four experimental runs (Fig.1 to 3 in Supplementary Materials), and its intensity is higher in run P7 for which the Xe content is higher (4 wt% *vs* 3 wt% for runs P5, P6 and P11). Amongst the atoms present in our melt composition (i.e. Si, Al, Na, K, O and H), only H and O are known to form compounds with Xe (see review by Haner and Schrobilgen (2015) and references therein). Xe-H bond length in Xe-O-H and Xe-C-H compounds is shorter, at 1.7-1.8 Å (Khriachtchev et al., 2008). Moreover, due to the very weak scattering factor of hydrogen, if the additional contribution at 2.05 Å was to be attributed to Xe-H, it would imply an extremely high coordination number. Theoretical calculations predict a much more comparable Xe-O bond length of 1.99 Å to 2.29 Å in Xe-doped SiO_2 quartz (Probert, 2010), and of 2.17 Å in Xe-doped fibrous SiO_2 (Kalinowski et al., 2014), two compounds chemically close to the present composition except for their crystalline state. The nature of the Xe-O bond is covalent for these predicted Xe-doped silica cristalline phases, as could also be expected from the sum of the covalent radii of oxygen (0.73 Å) and xenon (1.3 Å). Despite the absence

of reported compounds of Xe with Si, Al, Na and K, if Xe was to interact with these atoms in our experimental samples, one would expect an interatomic distance larger than 2.4 Å from covalent radii considerations. For these reasons, we attribute the newly observed peak at 2.05±0.05 Å to the Xe-O interatomic distance. Although no Xe-O contribution is distinct on ambient T data, whether before or after heating, a shoulder is still present on $g(r)$ around 2.00 Å unlike for the plain samples (Fig.3B), indicating a poorer ordering of Xe atoms. The second main difference between plain and Xe-doped HPG is the stronger intensity of the first sharp diffraction peak on $S(q)$ in the latter, which indicates an increase of the intermediate range order.

3.2. Xenon incorporation

In order to estimate the Xe-O coordination number, each particular ion i-ion j partial distribution function was simulated with the following equations:

$$g_{i,j}(r) = \frac{A_{i,j}}{nS_\infty \sigma_i \sqrt{2\pi}} exp\left(-\frac{(r-d_{i,j})^2}{2\sigma_{i,j}^2}\right) \tag{2}$$

$$A_{i,j} = \frac{CN_{i,j}}{\int \frac{4\pi r^2}{\sigma_i\sqrt{2\pi}} exp\left(\frac{-(r-d_{i,j})^2}{2\sigma_i^2}\right) dr} \tag{3}$$

where CN_i is the coordination number of the ion i-ion j contribution, $d_{i,j}$ the corresponding inter-atomic distance, and $\sigma_{i,j} = k\sqrt{d_{i,j}}$ a parameter depending on structural disorder (Hosemann and Bagchi, 1962) where k is an adjustable parameter (typically 0.08-0.15).

$$S(q) = n\sum_{i,j} c_i c_j f_{i,j}(q) \int_0^\infty r(g_{i,j}(r)-1)\frac{\sin(qr)}{k}\, dr \tag{4}$$

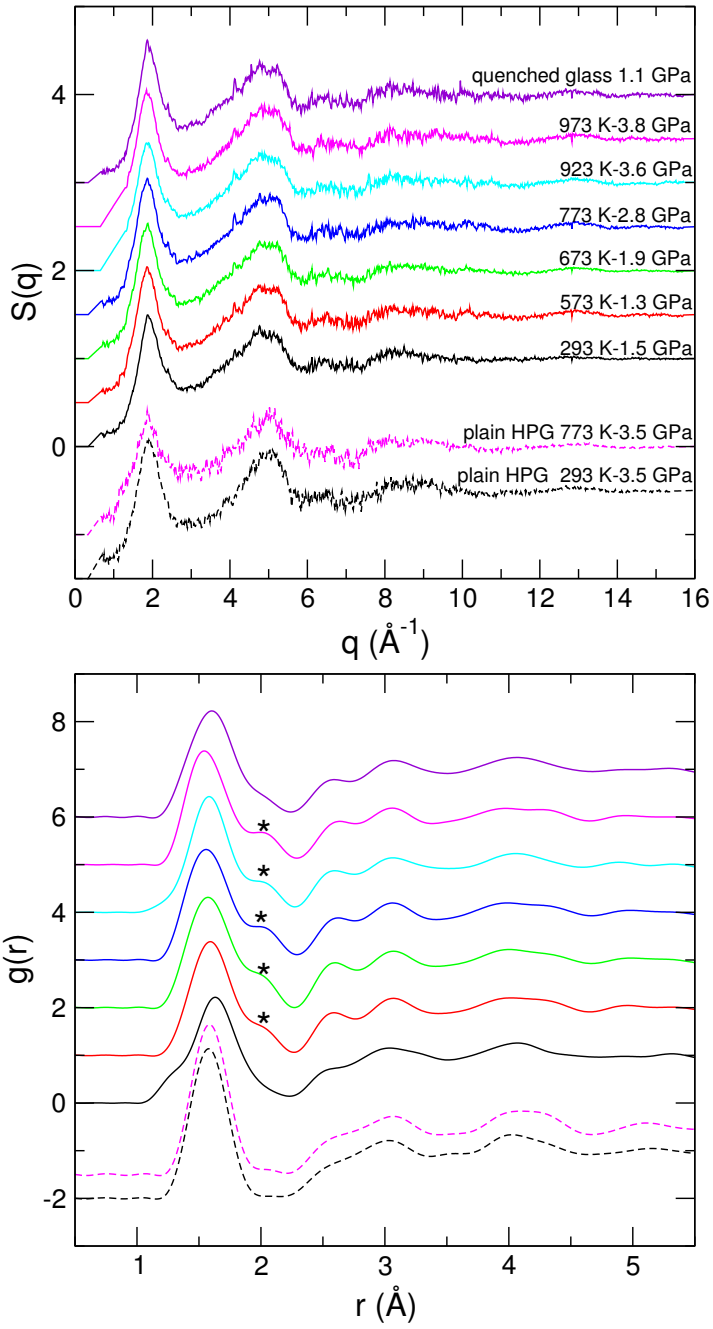

Figure 3: Structure factors, $S(q)$, of molten haplogranite at high pressures (top panel: runP6, see Supplementary Materials for runs P5, P7 and P11), and corresponding radial distribution functions, $g(r)$ (bottom panel). The dotted lines correspond to the plain sample and the full lines to the Xe-doped sample. The asterisk denotes the additional contribution observed for Xe-doped samples, and attributed to the Xe-O bond.

with

$$f_{i,j}(q) = \frac{f_i(q) f_j(q)}{\left[\sum_i c_i f_i(q)\right]^2} \quad (5)$$

where c_i is the mole fraction of species i, and f_i is the atomic scattering factor tabulated from Hajdu (1972). Following the approximation adopted by Eggert et al. (2002) for polyatomic liquids, the dependency of $f_{i,j}(q)$ on q can be removed in equation 4 and the experimental $g(r)$ simulated directly against the weighted sum of all individual $g_{i,j}$.

Ion-ion contributions at distances larger than 2.5 Å such as K-O and Si-Si are considered negligible below the Xe-O contribution (less than 5% of the peak height), and therefore only Si-O, Al-O, and Xe-O contributions were modelled as separate gaussians, along with a single common contribution for Na-O and O-O both circa 2.5 Å, and with signal at larger distances fitted as a single large contribution (Fig.4). Both Si-O and Al-O contribute to the first peak in $g(r)$, while the Al content is much smaller than the Si content. Consequently, it is not possible to refine independently both Si-O and Al-O contributions. Instead, we fixed the Al-O bond length to 1.77 Å (Drewitt et al., 2015), and its coordination number to either 4.0 up to 1 GPa or 4.3 above 1 GPa. Al-O CN is indeed expected to vary between 4.0 and 4.3 in our experimental 0 GPa-3.8 GPa P-range (Drewitt et al., 2015), and using either of these values provides a conservative estimate of the consequent error on the fitted Si-O coordination number of 0.05, with no significant effect on the fitted Xe-O coordination number. Fitted parameters CN_i, $d_{i,j}$, and k for Si-O, Al-O and Xe-O contributions at each P-T condition are given in Table 3. For the plain sample (run P3), the fitted CN and bond length (respectively

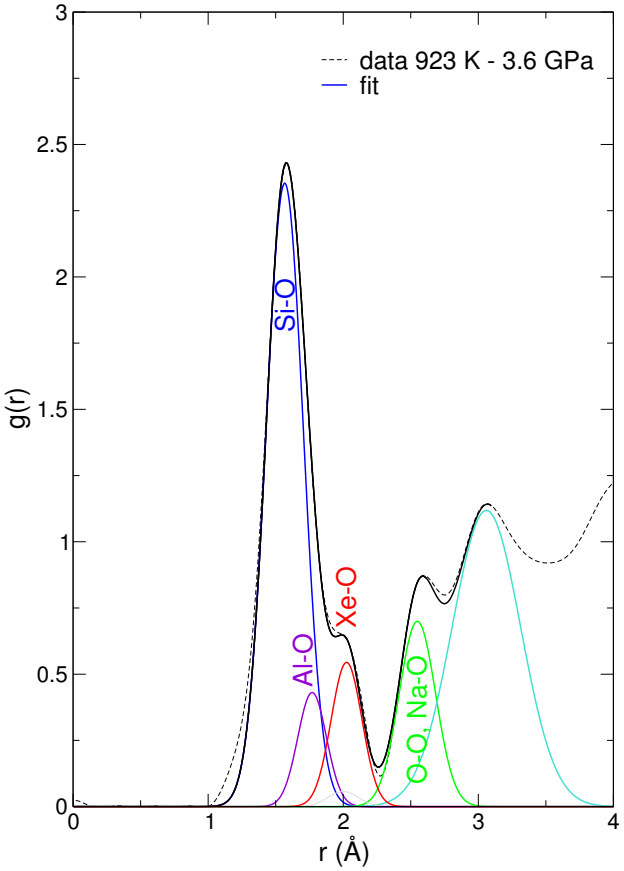

Figure 4: Fit to the experimental radial distribution function, $g(r)$. The black line is the sum of the underlying gaussians; only Si-O, Al-O, and Xe-O contributions were modeled as separate gaussians, along with a common contribution for Na-O and O-O both circa 2.5 Å, and with signal at larger distances fitted as a single large contribution including K-O and Si-Si at 3.1 Å; the grey gaussian is the Mg-O contribution due to slight contamination (1.5 wt%, see section 2.1).

4.1 and 1.57 Å±0.02Å) for Si-O are consistent with values reported for SiO_2 glass at similar P, i.e. respectively 4.0 and 1.58 Å (Benmore et al., 2010). Except for the room T data, the fitted Xe-O coordination number is 12 ± 2, with no dependence on either T or P in the investigated P-T range. Noteworthy is the systematic shift of the fit Si-O bond length upon heating to lower distances compared to the plain sample patterns (cf Table 3). This reduction of the Si-O bond length is accompanied, although less systematically, by a decrease of the Si-O coordination number. This changes in the Si-O contribution might compensate the charge transfer between Xe and O atoms.

The high coordination number found here is not consistent with Xe substitution to Si as proposed for quartz in the deep crust (Sanloup et al., 2005; Probert, 2010). Instead, it is consistent with the insertion of Xe in melt rings structure. Amorphous silica is characterized by a broad distribution spread between four and eight-membered rings (Huang et al., 2012), with a characteristic ring size close to 6 in compressed SiO_2 melts (Guerette et al., 2015). The center of these 6-membered rings is surrounded by 6 oxygens in the ring plane at circa 2.2 Å (Guerette et al., 2015), with a second nearest shell of another 6 oxygens off plane. The presence of Xe could therefore stabilize the 6-membered rings of the melt network, hence explaining the observed increase in intermediate range order in the presence of Xe. The stronger intensity of the first sharp diffraction peak can indeed be interpreted as a narrowed distribution of ring sizes, with 6-membered rings being more prominent compared to the broader distribution present in the plain HPG melt. Noble gases enter the melt ring structure, and as a consequence are more soluble in highly polymerized siliceous melts (Carroll and Stolper, 1993). In

Table 3: Fitting parameters derived for Si-O and Xe-O ion-ion contributions for all runs; CN_i: coordination number, d_i: bond length, k_i: width parameter of Gaussian. Error bars for Si-O and Al-O variable parameters do not vary and are given in the top row, they do vary for Xe-O as this contribution varies between ambient T and high T.

run #	Si-O			Al-O		Xe-O		
P-T conditions	CN	d (Å)	k	CN	k	CN	d (Å)	k
error bars	0.25	0.02	0.002	-	0.01			
P3 (no Xe)								
293 K-3.5 GPa	4.10	1.57	0.092	4.3	0.08	-	-	-
773 K-3.5 GPa	4.10	1.57	0.092	4.3	0.08	-	-	-
P5 (3 wt% Xe)								
293 K-2.9 GPa	3.93	1.58	0.150	4.3	0.14	10.8(21)	2.05(2)	0.085
453 K-2.2 GPa	3.70	1.55	0.140	4.3	0.14	12.6(4)	2.03(2)	0.080
573 K-2.7 GPa	3.70	1.56	0.120	4.3	0.14	13.0(2)	2.05(2)	0.078
773 K- 3.7 GPa	3.75	1.53	0.145	4.3	0.14	12.9(2)	2.03(2)	0.080
quench 2.5 GPa	3.87	1.57	0.120	4.3	0.14	12.0(4)	2.06(2)	0.084
P6 (3 wt% Xe)								
293 K-1.5 GPa	3.75	1.62	0.120	4.0	0.12	4.1(5)	2.02(2)	0.100
573 K-1.3 GPa	4.03	1.57	0.120	4.3	0.09	10.3(4)	2.02(2)	0.080
673 K-1.9 GPa	4.00	1.56	0.120	4.3	0.08	12.4(2)	2.00(2)	0.080
773 K-2.8 GPa	4.10	1.55	0.120	4.3	0.08	13.8(2)	2.03(2)	0.080
923 K-3.4 GPa	4.06	1.57	0.110	4.3	0.08	12.7(3)	2.03(2)	0.080
973 K-3.8 GPa	3.87	1.54	0.110	4.3	0.08	13.4(2)	2.02(2)	0.080
quench 1.1 GPa	3.93	1.58	0.130	4.0	0.10	6.0(5)	2.01(2)	0.085
P7 (4 wt% Xe)								
293 K-0.5 GPa	3.55	1.58	0.133	4.0	0.14	12.2(7)	2.05(2)	0.085
483 K-0.45 GPa	3.55	1.54	0.138	4.0	0.14	11.5(2)	2.05(2)	0.080
573 K-0.13 GPa	3.55	1.55	0.132	4.0	0.14	12.0(2)	2.05(2)	0.080
673 K-0.4 GPa	3.61	1.55	0.137	4.0	0.14	13.3(2)	2.05(2)	0.080
P11 (3 wt% Xe)								
293 K-4.4 GPa	3.95	1.54	0.150	4.3	0.14	9.0(10)	2.07(4)	0.120
457 K-3.8 GPa	3.73	1.53	0.140	4.3	0.14	11.9(2)	2.05(2)	0.090
588 K-3.6 GPa	3.88	1.54	0.125	4.3	0.11	10.3(3)	2.10(2)	0.090
693 K-4.1 GPa	3.82	1.53	0.125	4.3	0.11	12.7(2)	2.08(2)	0.088
773 K-4.2 GPa	3.90	1.53	0.120	4.3	0.11	11.4(2)	2.07(2)	0.080

the case of Kr dissolved in vitreous silica (Wulf et al., 1999), the oxygen atoms lie at a significantly greater distance of 3.45 Å compared to the Xe-O distance of 2.05±0.05 Å found in the compressed silicate melts, consistent with Kr being a neutral species in vitreous silica. There are no experimental indications on the valence of Xe in silica-rich melts. Xe has a +5.08 valence in Xe-doped fibrous silica (Kalinowski et al., 2014), the closest crystalline analogue to our silica-rich melts in terms of chemical composition, with a coordination number of 4 and mean bond length of 2.17 Å. Amongst all reported Xe oxides, Xe valence varies from +2.89 in Xe-doped olivine for a coordination number of 3 and bond length circa 2.0 Å (Crépisson et al., 2018), to +8 for Xe in XeO_4 (coordination number of 4, bond length of 1.74 Å (Gundersen and Hedberg, 1970)) and $K_4Xe_3O_{12}$ perovskite (coordination number of 6, bond length of 1.77 Å (Britvin et al., 2016)). From this review, no systematic trend appears between Xe-O coordination number, valence and/or bond length; however the Xe-O bond always has a covalent character, and a minimum valence of +4 for Xe in compressed silicate melts seems a conservative assumption.

3.3. Xe solubility

Our measured solubility values of Xe at 3.5 GPa in molten hydrous HPG, i.e. 3.1(0.4) wt% for 7.2 wt% H_2O and 4.0(0.8) wt% for 5.1 wt% H_2O, are respectively 5 and 7 times higher than Xe solubility in tholeitic melt (Schmidt and Keppler, 2002). The lower solubility of Xe in the most hydrated HPG glass is consistent with noble gas solubility being highest in the most polymerized melts (Carroll and Stolper, 1993),

water being an effective depolymerizing agent in silicate melts. Similarly, Schmidt and Keppler (2002) reported Ar solubility values about 5 times higher in molten HPG than in molten tholeite. The experimental solubility values are however at odds with molecular dynamic calculations (Guillot and Sator, 2012), being a factor of 8 higher for Xe in tholeitic melt, and 10 higher for Xe in HPG melt (Fig.5). We propose that such a strong discrepancy is related to the chemical interaction between Xe and neighbouring O atoms that is not considered in theoretical calculations but likely enhances Xe solubility in silicate melts. Indeed, considering a neutral Xe atom implies a larger atomic radius than an oxidized Xe atom, hence the much lower abundance of sites large enough to accommodate neutral Xe atoms that does not match experimentally measured solubilities. Simulations allowing Xe to ionize would be expected to reproduce the solubility data. A structural investigation of Xe environment in basaltic melts using X-ray diffraction as done here for HPG melts is not possible, due to the low Xe solubility for this composition. The very weak Xe contribution to the pair distribution functions would indeed be below noise level. The similar mismatch between experimental and theoretical Xe solubility values in molten HPG and basalt nonetheless indicates that Xe oxidation may as well occur in basalts at depth.

4. Discussion

Xe oxidation in deep magmas and consequent isotopic fractionation may be expected in the following geodynamical settings. Xe oxidation can occur in major cristalline phases of the deep continental crust (Sanloup et al., 2005; Probert, 2010; Kalinowski

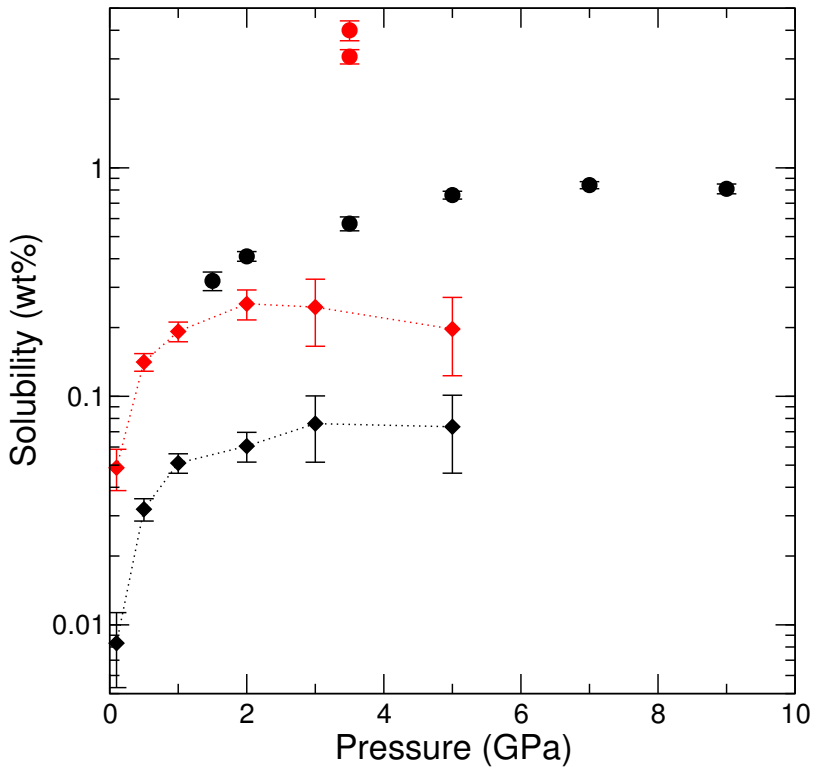

Figure 5: Experimental solubility data for Xe; black circles: in tholeitic melt (Schmidt and Keppler, 2002), red circles: in hydrous haplogranitic melts (this work). Are shown for comparison theoretical calculations by Guillot and Sator (2012) (black diamonds: tholeitic melt, red diamonds: haplogranitic melt).

et al., 2014) and upper mantle (Sanloup et al., 2011; Crépisson et al., 2018). The present experimental results show that Xe oxidation could also occur in magmas generated at subduction zones, following fluid and/or melt release from the subducted plate. Hydrous silicic slab-derived melts which composition is similar to ours occur either by melting of the basaltic crust (Prouteau et al., 2001) or by melting of siliceous sediments (Turner et al., 2012), the latter interestingly having a strong Xe retention (Matsuda and Matsubara, 1989). These melts and their metasomatic products are subsequently found in the continental lithosphere. Xe terrestrial deep cycle is therefore likely controlled by the behaviour of silica-rich materials (i.e. siliceous sediments, polymerized crustal melts and their crystallization products), providing a storage mechanism in these materials at depth. Geochemical tracing of Xe also suggests that Xe is stored in the continental lithosphere (Broadley et al., 2016), including in the deep crust where elemental and isotopic excesses have been reported (Pujol et al., 2011; Holland et al., 2013). Besides deep crustal melts, other obvious Xe reservoirs at depth would be melts trapped at depth as probed by seismological data atop the 410 km (Tauzin et al., 2010), below the 670 km (Schmandt et al., 2014) and at the core-mantle boundary (Garnero and McNamara, 2008). The latter might be a remnant of the magma ocean, in which noble gases were dissolved (Harper, 1996), explaining the deep mantle signature of heavy noble gases. Subsequent atmosphere ejection (T-Tauri blow-off and impact erosion) resulted in the Xe present-day atmospheric signature being derived from the Xe fraction retained at depth.

Xe isotopes are highly fractionated in both terrestrial and martian atmospheres, by

30 ‰/amu. Isotopic fractionation in experimental samples remains to be measured in order to quantitatively assess how Xe oxydation at depth may solve the Xe isotopic paradox. However, experiments involving noble gas ionization resulted in mass dependent isotope fractionation of Xe of the order of 5-15 ‰/amu favouring heavy isotopes at 1000 K (Kuga et al., 2015). This contradicts the intuition that elements are not isotopically fractionated at high T, as also shown by nitrogen isotopes in metal/melt partitioning experiments with $\delta^{15}N = -3.5 \pm 1.7$‰ even in the 1900-2100 K range (Li et al., 2016). From bond stiffness considerations, the effect of Xe-O bond formation in silicates is expected to be stronger than simple ionization as it involves more charge transfer ($0 \rightarrow 4$, cf section 3.2) than simple ionization while occurring at similar T (circa 1000 K). Xe oxydation in crystalline silica occurs in a different environment, with Xe being bonded to four oxygen atoms in a planar geometry (Probert, 2010; Kalinowski et al., 2014). Different bonding environment in crystals and melts may also induce isotopic fractionation, that unlike elemental fractionation, should be preserved in experimental high P-T samples quenched back to ambient conditions.

5. Conclusions

From *in situ* high energy X-ray diffraction measurements on compressed silicate melts, it is shown that Xe bonds to oxygen in hydrous haplogranitic magmas at depth. The Xe-O bond length is 2.05±0.05 Å and its coordination number of 12 ± 2, consistent with Xe insertion in 6-membered rings, with 6 oxygen in the ring plane and 6 oxygen off plane. The Xe-O bond is evidenced on pair distribution functions that describe

the melt structure, while it is absent for Xe undoped melt. This result provides an explanation for the order of magnitude difference between experimentally measured and theoretically calculated Xe solubility in melts, while the results are in much better agreement for Ar.

This result adds to previous studies on Xe retention in minerals at depth, comforting the hypothesis of Xe storage at depth to explain the 'missing Xe' paradox. To what extent Xe retention in silicate minerals and melts affects its partitioning in magmatic processes depends on crystal/melt partition coefficients. Measuring Xe crystal/melt partitioning on samples quenched to ambient conditions has proved challenging, as demonstrated by the results spanning 7 orders of magnitude (Heber et al., 2007). Instead, a comprehensive understanding of Xe environment in melts and major silicate minerals would help to provide a theoretical framework to model Xe partitioning. This method was initially proposed by Brooker et al. (2003), although the authors then assumed zero charge neutrality for Xe, and would need to be revised to consider Xe oxidation and the consequent smaller radius of Xe.

This study therefore paves the way for a more systematic study of Xe chemical environment in planetary materials, extended to crystalline phases. Understanding the chemical environment of noble gases in planetary materials seems the most efficient path to solve the fundamental geochemistry of xenon.

6. Acknowledgements

We acknowledge M. Fialin for assistance with the electron microprobe analyses, and H. Khodja and S. Surblé for assistance with the nuclear microprobe analyses. Portions of this research were carried out at the light source PETRA III at DESY, a member of the Helmholtz Association (HGF). This work was supported by the European Community's Seventh Framework Programme (FP7/2007-2013) under grant agreements no. 312284 and 259649 (European Research Council starting grant to C.S.), and from French state funds managed by the ANR within the Investissements d'Avenir programme under reference ANR-11-IDEX-0004-02 (cluster of Excellence MATISSE led by Sorbonne Universités).

7. References

Allègre, C. J., Staudacher, T., Sarda, P., 1986. Rare gas systematics: formation of the atmosphere, evolution and structure of the earth's mantle. Earth Planet. Sci. Lett. 81, 127–150.

Anders, E., Owen, T., 1977. Mars and Earth: Origin and abundance of volatiles. Science 198, 453–465.

Avice, G., Marty, B., 2014. The iodine-plutonium-xenon age of the Moon-Earth system revisited. Phil. Trans. R. Soc. A 372, 20130260.

Benmore, C. J., Soignard, E., Amin, S. A., Guthrie, M., Shastri, S. D., Lee, P. L., Yarger, J. L., 2010. Structural and topological changes in silica glass at pressure. Phys. Rev. B 81, 054105.

Boehnke, P., Caffee, M. W., Harrison, T. M., 2015. Xenon isotopes in the MORB source, not distinctive of early global degassing. Geophys. Res. Lett. 42, 4367–4374.

Boettcher, S. L., Guo, Q., Montana, A., 1989. A simple device for loading gases in high-pressure experiments. Am. Mineral. 74, 1383–1384.

Britvin, S. N., Kashtanov, S. A., Krivovichev, S. V., Chukanov, N. V., 2016. Xenon in Rigid Oxide Frameworks: Structure, Bonding and Explosive Properties of Layered Perovskite $K_4Xe_3O_12$. J. Am. Chem. Soc. 138 (42), 13838–13841.

375 Broadley, M. W., Ballentine, C. J., Chavrit, D., Dallai, L., Burgess, R., 2016. Sedi-
376 mentary halogens and noble gases within Western Antarctic xenoliths: Implications
377 of extensive volatile recycling to the sub continental lithospheric mantle. Geochim.
378 Cosmochim. Acta 176, 139–156.

379 Brock, D. S., Schrobilgen, G. J., 2011. Synthesis of the missing oxide of xenon, XeO_2,
380 and its implications for Earth's missing xenon. J. Am. Chem. Soc. 133, 6265–6269.

381 Brooker, R. A., Du, Z., Blundy, J. D., Kelley, S. P., Allan, N. L., Wood, B. J., Chamorro,
382 E. M., Wartho, J.-A., Purton, J. A., 2003. The 'zero charge' partitioning behaviour
383 of noble gases during mantle melting. Nature 423, 738–741.

384 Bureau, H., Foy, E., Raepsaet, C., Somogyi, A., Munsch, P., Simon, G., Kubsky, S.,
385 2010. Bromine cycle in subduction zones through in situ Br monitoring in diamond
386 anvil cells. Geochim. Cosmochim. Acta 74, 3839–3850.

387 Bureau, H., Keppler, H., Métrich, N., 2000. Volcanic degassing of bromine and iodine:
388 Experimental fluid/melt partitioning data and applications to stratospheric chem-
389 istry. Earth Planet. Sci. Lett. 183, 51–60.

390 Bureau, H., Raepsaet, C., Khodja, H., Carraro, A., Aubaud, C., Kubsky, S., 2009.
391 Determination of hydrogen content in geological samples using elastic recoil detection
392 analysis (ERDA). Geochim. Cosmochim. Acta 73, 3311–3322.

393 Caffee, M. W., Hudson, G. B., Velsko, C., Huss, G. R., Alexander, E. C. J., Chivas,

394 A. R., 1999. Primordial noble gases from Earth's mantle: Identification of a primitive
395 volatile component. Science 285, 2115–2118.

396 Carroll, M., Stolper, E., 1993. Noble gas solubilities in silicate melts and glasses: New
397 experimental results for argon and the relationship between solubility and ionic poros-
398 ity. Geochim. Cosmochim. Acta 57, 5039–5051.

399 Crépisson, C., Blanchard, M., Lazzeri, M., Balan, E., Sanloup, C., 2018. New con-
400 straints on Xe incorporation mechanisms in olivine from first-principles calculations.
401 Geochim. Cosmochim. Acta 222, 146–155.

402 Dauphas, N., 2003. The dual origin of the terrestrial atmosphere. Icarus 165, 326–333.

403 de Grouchy, C. J. L., Sanloup, C., Cochain, B., Drewitt, J. W. E., Kono, Y., Crépisson,
404 C., 2017. Lutetium incorporation in magmas at depth: changes in melt local envi-
405 ronment and the influence on partitioning behaviour. Earth Planet. Sci. Lett. 464,
406 155–165.

407 Dewaele, A., Worth, N., Pickard, C. J., Needs, R. J., Pascarelli, S., Mathon, O.,
408 Mezouar, M., Irifune, T., 2016. Synthesis and stability of xenon oxides Xe_2O_5 and
409 Xe_3O_2 under pressure. Nature Chemistry 8 (8), 784–790.

410 Dingwell, D. B., 1998. The glass transition in hydrous granitic melts. Phys. Earth
411 Planet. Int. 107, 1–8.

412 Drewitt, J. W. E., Jahn, S., Sanloup, C., de Grouchy, C., Garbarino, G., Hennet, L.,

2015. Development of chemical and topological structure in aluminosilicate liquids and glasses at high pressure. J. Phys.: Cond. Matt. 27, 105103.

Eggert, J. H., Weck, G., Loubeyre, P., Mezouar, M., 2002. Quantitative structure factor and density measurements of high-pressure in diamond anvil cells by x-ray diffraction: Argon and water. Phys. Rev. B 65, 174105.

Fei, Y., van Orman, J., Li, J., van Westrenen, W., Sanloup, C., Minarik, W., Hirose, K., Komabayashi, T., Walter, M., Funakoshi, K., 2004. Experimentally determined postspinel transformation boundary in Mg_2SiO_4 using MgO as an internal pressure standard and its geophysical implications. J. Geophys. Res. 109, B02305.

Garnero, E. J., McNamara, A. K., 2008. Structure and dynamics of Earth's lower mantle. Science 320, 626–628.

Gilmour, J. D., Whitby, J. A., Turner, G., 1998. Xenon isotopes in irradiated alh84001: Evidence for shock-induced trapping of ancient martian atmosphere. Geochim. Cosmochim. Acta 62, 2555–2571.

Guerette, M., Ackerson, M. R., Thomas, J., Yuan, F., Watson, E. B., Walker, D., Huang, L., OCT 15 2015. Structure and Properties of Silica Glass Densified in Cold Compression and Hot Compression. Scientific Reports 5.

Guillot, B., Sator, N., 2012. Noble gases in high-pressure silicate liquids: A computer simulation study. Geochim. Cosmochim. Acta 80, 51–69.

Gundersen, G., Hedberg, K., 1970. Molecular structure of xenon tetroxide, XeO_4. J. Chem. Phys. 52, 812–815.

Hajdu, F., 1972. Revised parameters of the analytic fits for coherent and incoherent scattered x-ray intensities of the first 36 atoms. Acta Cryst., 250–252.

Hammersley, A. P., Svensson, S. O., Hanfland, M., Fitch, A. N., Hausermann, D., 1996. Two-dimensional detector software: From real detector to idealised image or two-theta scan. High Press. Res. 14, 235–248.

Haner, J., Schrobilgen, G. J., 2015. The chemistry of Xenon. Chem. Rev. 115, 1255–1295.

Harper, C. L., 1996. Evidence for ^{92g}Nb in the early solar system and evaluation of a new p-process cosmochronometer from ^{92g}Nb/^{92}Mo. ApJ 466, 437–456.

Heber, V. S., Brooker, R. A., Kelley, S. P., Wood, B. J., 2007. Crystal-melt partitioning of noble gases (helium, neon, argon, krypton, and xenon) for olivine and clinopyroxene. Geochim. Cosmochim. Acta 71, 1041–1061.

Hermann, A., Schwerdtfeger, P., 2014. Xenon suboxides stable under pressure. J. Phys. Chem. Lett. 5, 4336–4342.

Holland, G., Ballentine, C. J., 2006. Seawater subduction controls the heavy noble gas composition of the mantle. Nature 441, 186–191.

Holland, G., Lollar, B. S., Li, L., Lacrampe-Couloume, G., Slater, G. F., Ballentine,

C. J., 2013. Deep fracture fluids isolated in the crust since the Precambrian era. Nature 497, 357–360.

Hosemann, R., Bagchi, S. N., 1962. Direct Analysis of Diffraction by Matter. North-Holland, Amsterdam.

Hourdin, F., Issartel, J.-P., 2000. Sub-surface nuclear tests monitoring through the CTBT xenon network. Geophys. Res. Lett. 27, 2245–2248.

Huang, P. Y., Kurasch, S., Srivastava, A., Skakalova, V., Kotakoski, J., Krasheninnikov, A. V., Hovden, R., Mao, Q., Meyer, J. C., Smet, J., Muller, D. A., Kaiser, U., 2012. Direct imaging of a two-dimensional silica glass on graphene. Nano Letters 12 (2), 1081–1086.

Kalinowski, J., Rasanen, M., Gerber, R. B., 2014. Chemically-bound xenon in fibrous silica. Phys. Chem. Chem. Phys. 16, 11658–11661.

Khriachtchev, L., Isokoski, K., Cohen, A., Räsänen, M., Gerber, R. B., 2008. A small neutral molecule with two noble-gas atoms: HXeOXeH. J. Am. Chem. Soc. 130, 6114–6118.

Kleine, T., Münker, C., Mezger, K., Palme, H., 2002. Rapid accretion and early core formation on asteroids and the terrestrial planets from Hf-W chronometry. Nature 418, 952–955.

Krummenacher, D., Merrihue, C. M., Pepin, R. O., Reynolds, J. H., 1962. Meteoritic

krypton and barium versus the general isotopic anomalies in xenon. Geochim. Cosmochim. Acta 26, 231–249.

Kuga, M., B.Marty, Marrocchi, Y., Tissandier, Y., 2015. Structure and hydrogen ordering in ices vi, vii and viii by neutron powder diffraction. Proc. Natl. Acad. Sci. U.S.A. 112, 7129–7134.

Lee, K. M., Steinle-Neumann, G., 2006. High-pressure alloying of iron and xenon: "Missing" Xe in the Earth's core? J. Geophys. Res. 111, B02202.

Li, Y., Marty, B., Shcheka, S., Zimmermann, L., Keppler, H., 2016. Nitrogen isotope fractionation during terrestrial core-mantle separation. Geochem. Persp. Let. 2, 138–147.

Malfait, W. J., Seifert, R., Petitgirard, S., Perrillat, J.-P., Mezouar, M., Ota, T., Nakamura, E., Lerch, P., Sanchez-Valle, C., 2014. Supervolcano eruptions driven by melt buoyancy in large silicic magma chambers. Nat. Geoscience 7, 122–125.

Mao, H. K., Xu, J., Bell, P. M., 1986. Calibration of the ruby pressure gauge to 800 kbar under quasi-hydrostatic conditions. J. Geophys. Res. 91, 4673–4676.

Marty, B., Altwegg, K., Balsiger, H., Bar-Nun, A., Bekaert, D. V., Berthelier, J.-J., Bieler, A., Briois, C., Calmonte, U., Combi, M., ad B. Fiethe, J. D. K., Fuselier, S., Gasc, S., Gombosi, T. I., Hansen, K. C., Hässig, M., Jäckel, A., Kopp, E., Korth, A., Roy, L. L., Mall, U., Mousis, O., Owen, T., Rème, H., Rubin, M., Sémon, T., Tzou,

C.-Y., Waite, J. H., Wurz, P., 2017. Xenon isotopes in 67P/Churyumov-Gerasimenko show that comets contributed to Earth's atmosphere. Science 356, 1069–1072.

Matsuda, J.-I., Matsubara, K., 1989. Noble gases in silica and their implication for the terrestrial 'missing' Xe. Geophys. Res. Lett. 16, 81–84.

Montana, A., Guo, Q., Boettcher, S., White, B. S., Brearley, M., 1993. Xe and Ar in high-pressure silicate liquids. Am. Mineral. 78, 1135–1142.

Ozima, M., Miura, Y., Podosek, F., 2002. Revisiting I-Xe systematics, an early solar system chronometer. Geochim. Cosmochim. Acta 66 (15A, 1), A576.

Ozima, M., Podosek, F. A., 1999. Formation age of Earth from $^{129}I/^{127}I$ and $^{244}Pu/^{238}U$ systematics and the missing Xe. J. Geophys. Res. 104, 25493–25499.

Pepin, R. O., 2006. Atmospheres on the terrestrial planets: Clues to origin and evolution. Earth Planet. Sci. Lett. 252, 1–14.

Probert, M. I. J., 2010. An ab initio study of xenon retention in α-quartz. J. Phys.:Condens. Matter 22, 025501.

Prouteau, G., Scaillet, B., Pichavant, M., Maury, R., 2001. Evidence for mantle metasomatism by hydrous silicic melts derived from subducted oceanic crust. Nature 410 (6825), 197–200.

Pujol, M., Marty, B., Burgess, R., 2011. Chondritic-like xenon trapped in Archean

507 rocks: A possible signature of the ancient atmosphere. Earth Planet. Sci. Lett. 308,
508 298–306.

509 Sanloup, C., Bonev, S. A., Hochlaf, M., Maynard-Casely, H. E., 2013. Reactivity of
510 xenon with ice at planetary conditions. Phys. Rev. Lett. 110, 265501.

511 Sanloup, C., Schmidt, B. C., Gudfinnsson, G., Dewaele, A., Mezouar, M., 2011. Xenon
512 and argon: a contrasting behavior in olivine at depth. Geochim. Cosmochim. Acta
513 75, 6271–6284.

514 Sanloup, C., Schmidt, B. C., Perez, E. C., Jambon, A., Gregoryanz, E., Mezouar, M.,
515 2005. Retention of xenon in quartz and Earth's missing xenon. Science 310, 1174–
516 1177.

517 Schmandt, B., Jacobsen, S. D., Becker, T. W., Liu, Z. K., Dueker, K. G., 2014. Dehy-
518 dration melting at the top of the lower mantle. Science 344, 1265–1268.

519 Schmidt, B., Keppler, H., 2002. Experimental evidence for high noble gas solubilities
520 in silicate melts under mantle pressures. Earth Planet. Sci. Lett. 195, 277–290.

521 Seoung, D., Lee, Y., Cynn, H., Park, C., Choi, K.-Y., Blom, D., Evans, W. J., Kao,
522 C.-C., Vogt, T., Lee, Y., 2014. Irreversible xenon insertion into a small-pore zeolite
523 at moderate pressures and temperatures. Nat. Chem. 6, 835–839.

524 Staudacher, T., Allègre, C. J., 1982. Terrestrial xenology. Earth Planet. Sci. Lett. 60,
525 389–405.

526 Swindle, T. D., Caffe, M. W., Hohenberg, C. M., 1986. Xenon and other noble gases in
527 shergottites. Geochim. Cosmochim. Acta 50, 1001–1015.

528 Tauzin, B., Debayle, E., Wittlinger, G., 2010. Seismic evidence for a global low-velocity
529 layer within the Earth's upper mantle. Nature Geoscience 3, 718–721.

530 Trieloff, M., Kunz, J., 2005. Isotope systematics of noble gases in the Earth's mantle:
531 possible sources of primordial isotopes and implications for mantle structure. Phys.
532 Earth. Planet. Int. 148, 13–38.

533 Turner, S., Caulfield, J., Turner, M., van Keken, P., Maury, R., Sandiford, M.,
534 Prouteau, G., JAN 2012. Recent contribution of sediments and fluids to the mantle's
535 volatile budget. Nature Geoscience 5 (1), 50–54.

536 Wulf, R., Calas, G., Ramos, A., Büttner, H., Roselieb, K., Rosenhauer, M., 1999.
537 Structural environment of krypton dissolved in vitreous silica. Amer. Min. 84, 1461–
538 1463.

539 Zhu, L., Liu, H., Pickard, C. ., Zou, G., Ma, Y., 2014. Reactions of xenon with iron
540 and nickel are predicted in the Earth?s inner core. Nat. Chem. 6, 645–649.

541 Zhu, Q., Jung, D. Y., Oganov, A. R., Glass, C. W., Gatti, C., Lyakhov, A. O., 2013.
542 Stability of xenon oxides at high pressures. Nat. Chem. 5, 61–65.